Earth Planet. Sci. Lett. 634 (2024) 118678

Contents lists available at ScienceDirect

Earth and Planetary Science Letters

journal homepage: www.elsevier.com/locate/epsl

Neoproterozoic low-*T*/*P* metamorphism in the Yangtze Block manifests a long-lived subduction girdle around Rodinia

Jun-Yong Li [a], Xiao-Lei Wang [a,*], Peter A. Cawood [b], Zhi-Dong Gu [c], Yue Guan [a]

[a] State Key Laboratory for Mineral Deposits Research, Frontiers Science Center for Critical Earth Material Cycling, School of Earth Sciences and Engineering, Nanjing University, Nanjing, 210023, China
[b] School of Earth Atmosphere and Environment, Monash University, Melbourne, Vic, 3800, Australia
[c] Research Institute of Petroleum Exploration and Development, PetroChina, Beijing, 10083, China

ARTICLE INFO

Keywords:
Yangtze block
Low-*T*/*P* metamorphism
Rodinia supercontinent
Phengite
Accretionary orogenesis
Long-lived subduction

ABSTRACT

Identifying long-lived subduction at the periphery of supercontinents provides insights into the processes of block assembly and dispersal within the supercontinent cycle. The Yangtze Block of South China stands as a key component during the transition from Rodinia to Gondwana, characterized by active tectono-magmatic processes throughout the early to middle Neoproterozoic. However, the lack of metamorphic records associated with accretionary orogenesis results in ambiguity about the tectonic regime and its evolution in Rodinia during this period. Here, we present evidence of low-temperature/pressure ratio (low-*T*/*P*) metamorphism in phengite-bearing orthogneisses from the western margin of the Yangtze Block (WYB). Through petrographic investigations and zircon U–Pb–Hf–O isotopic analysis in core and rim domains, we identify two distinct metamorphic rock types, with protolith ages of 1419 ± 19 Ma and 831 ± 9 Ma. Both rock types record metamorphism at ca. 830–820 Ma, accompanied by infiltration of externally-derived melts with high-$\delta^{18}O$ and unradiogenic Hf isotopes. Our phase equilibria modeling, combined with mineral thermometry and *Si*-in-phengite content, shows peak metamorphic conditions of ~550 °C and ~8.2–8.6 kbar, corresponding to a cold geothermal gradient (19.0–20.5 °C/km). The low-*T*/*P* metamorphism is interpreted to occur either in a subduction zone accretionary wedge or in an overriding forearc continental crust, providing robust evidence for Neoproterozoic orogenesis of the WYB within a subduction framework. Based on petrological, isotopic, and paleomagnetic data, we conclude that the WYB represents part of a long-lived subduction girdle (at least ca. 970–750 Ma) at the periphery of Rodinia. Since the early stage of Rodinia breakup, this girdle was involved in alternating advance and retreat accretionary orogenesis as the Yangtze Block continuously drifted away from a mantle upwelling toward the degree-2 girdle of mantle downwelling. Our study provides a snapshot of the evolution of a complete long-lived circum-Rodinian subduction girdle during the transition from Rodinia to Gondwana.

1. Introduction

The Neoproterozoic Era is an important transition period, that witnessed a change from mid-Proterozoic orogenic slowdown or quiescence (Sobolev and Brown, 2019; Tang et al., 2021), or ubiquitous hot, thin orogenesis (Spencer et al., 2021) to a regime characterized by active modern-style plate tectonics involving low-temperature/pressure ratio (low-*T*/*P*) conditions and therefore comparatively cold thermal gradients (e.g., Cawood and Hawkesworth, 2014; Stern, 2018, 2020). Abundant subduction-diagnostic rocks in the metamorphic record from this period, such as ophiolites, blueschists, and "cold" eclogites, imply that modern-style plate tectonics was occurring (Stern, 2018; Brown et al., 2020; Cawood et al., 2022). In this era, Earth's tectonics were dominated by the breakup of Rodinia and the transition to the assembly of Gondwana (e.g., Li et al., 2008; Cawood et al., 2016), where the mantle structure was thought to be dominated by degree-2 convection (two antipodal upwellings bisected by a meridional downwelling) (Zhong et al., 2007; Wang et al., 2021; Cawood et al., 2021; Martin et al., 2024). Within the context of this degree-2 mantle structure, the Rodinia supercontinent, whose core is thought to have assembled through collisional processes involving Laurentia, Amazonia, and Batica at ca. 1100–980 Ma (e.g., Johansson, 2009; Hynes and Rivers, 2010; Cawood and Pisarevsky, 2017), was located over one mantle upwelling and broke up mainly after 900 Ma (e.g., Li et al., 2008; Cawood et al., 2021).

* Corresponding author.
E-mail address: wxl@nju.edu.cn (X.-L. Wang).

https://doi.org/10.1016/j.epsl.2024.118678
Received 6 April 2023; Received in revised form 6 March 2024; Accepted 15 March 2024

During the breakup, continental blocks at Rodinia's outer periphery were interpreted to successively incorporate into subduction-accretionary orogenesis (Cawood et al., 2016) and expand to align with the great circle of mantle downwelling (Cawood et al., 2021). These circum-Rodinian subduction girdles were generally long-lived (≥ 100 m.y.) and have been recorded in many continental blocks such as northwestern India (ranging from at least 1000 Ma to 820 Ma; Zhao et al., 2018), West Africa (ca. 880–680 Ma; Konopásek et al., 2018), Tarim (ca. 950–600 Ma; Ge et al., 2014), Seychelles and northern Madagascar (ca. 800–700 Ma; Ashwal et al., 2002) , and Cadomia and Avalonia (ca. 760–570 Ma; Murphy et al., 2013, and references therein). When the dispersing continents arrived at the mantle downwelling zone, it is thought they progressively converge to form Gondwana over the locus of downwelling (Wang et al., 2021), and that a complete long-lived subduction girdle around Rodinia was necessary for its ultimate breakup and the transition to the Gondwana assembly (Cawood et al., 2016, 2021).

The Yangtze Block in the northwestern part of the South China Block is recognized as a key element of supercontinent reconstructions throughout the Neoproterozoic (ca. 1000–540 Ma) (Fig. 1A; Li et al., 1995, 2008; Zhou et al., 2002; Merdith et al., 2017; Cawood et al., 2018) and is characterized by widespread Neoproterozoic magmatism and sedimentation (Fig. 1A; e.g., Zhao and Cawood, 2012). However, whether it constituted part of a subduction girdle around Rodinia is unclear, given tectonic models for the period between ca. 860–750 Ma invoke either vertical tectonics associated with (super) plume-dynamics (e.g., Li et al., 1999, 2003; Zou et al., 2021) or horizontal orogenic processes linked with oceanic-continent subduction (e.g., Zhou et al., 2002; Zheng and Zhang, 2007; Cawood et al., 2020; Zhao et al., 2021). The plume-dynamics model advocates that the Yangtze Block in the

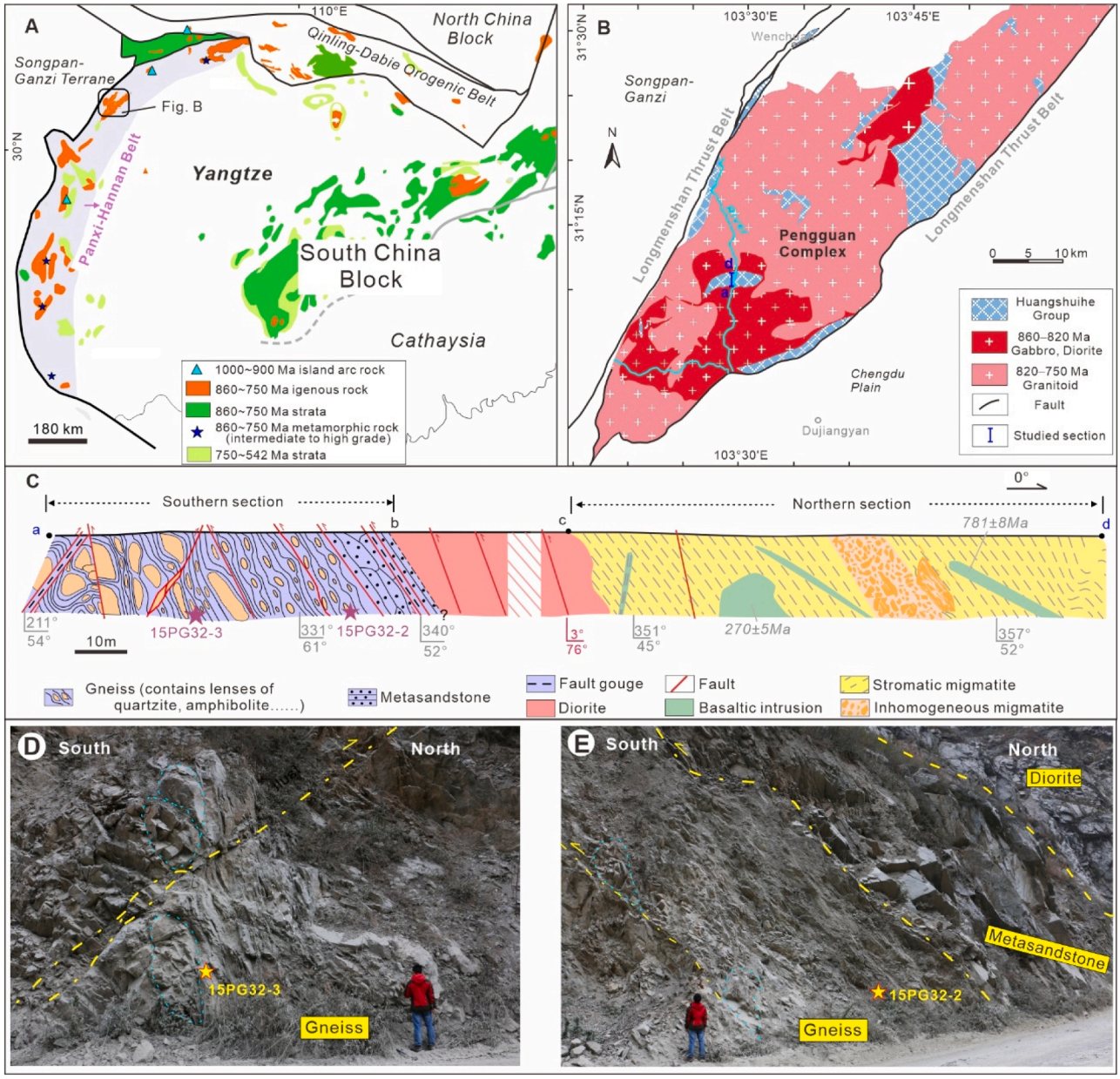

Fig. 1. Geological map and field photos of the investigated samples. (A) Simplified geologic map (modified after Zhao and Cawood, 2012) showing widespread ca. 860–750 Ma strata and igneous rocks, plus sporadically exposed ca. 970–900 Ma island arc rocks and ca. 880–760 Ma metamorphic rocks in the Yangtze Block. (B) Detailed map of the Pengguan Complex, Huangshuihe Group, and location of studied section (a-d). (C) Cross section (a-d) showing different lithologies between southern and northern sections, and sample locations. (E–F) Orthogneiss samples taken in the field are marked with yellow stars. Cyan dotted lines denote lenses of rock. More field photos of the studied section are shown in Fig. S1.

interior of Rodinia is part of the missing link between Australia-East Antarctica and Laurentia (e.g., Li et al., 1995), while the horizontal orogeny model places the Yangtze Block at the periphery of Rodinia and near India and Australia (e.g., Cawood et al., 2018). Part of this uncertainty relates to a lack of studies constraining the Neoproterozoic metamorphic pressure and temperature conditions. This is due in part to the fact that most of the exposed Neoproterozoic rocks record up-to-greenschist facies metamorphism (e.g., Zhao and Cawood, 2012) and also because Neoproterozoic deep-crustal rocks are largely covered by Phanerozoic sedimentary rocks (e.g., Gu et al., 2014).

In this study, we identified two types of orthogneiss with metamorphic ages of ca. 830–820 Ma from a Neoproterozoic deep-crustal section in the western margin of Yangtze Block (WYB). We documented their petrology, geochronology, and geochemistry to unravel their metamorphic histories and tectonic settings. By compiling petrological, isotopic, and paleomagnetic data, we demonstrate the evolution of Neoproterozoic orogenic system on WYB within the context of Rodinia's assembly and breakup.

2. Geological context

The Yangtze Block consists of an Archean–Paleoproterozoic basement surrounded by Neoproterozoic orogenic belts (Zhao and Cawood, 2012). It is separated from the Cathaysia Block to the southeast by the Neoproterozoic Jiangnan Orogen, from the North China Block to the north by the Triassic Qinling-Dabie Orogenic Belt, and from the Tibetan Plateau to the west by the Triassic Songpan-Ganzi Terrane (Fig. 1A). It witnessed significant crustal growth and reworking during ca. 970–750 Ma (e.g., Wang et al., 2007; Zhao and Cawood, 2012) and extensive sedimentation during ca. 750–542 Ma (e.g., Shu et al., 2021) (Fig. 1A). The Panxi-Hannan Belt, which delineates the western and northwestern margins of the Yangtze Block, records active tectono-magmatic processes mainly from ca. 860 to ca. 750 Ma (Fig. 1A; Zhao et al., 2021 and reference therein). The belt hosts a series of linearly-distributed ca. 860–750 Ma metamorphic-plutonic complexes which have been interpreted to represent middle- to upper-crustal sections (e.g., Wang et al., 2020; Li et al., 2021a; Zhu et al., 2023). These metamorphic-plutonic complexes are characterized by voluminous felsic intrusions with minor mafic–ultramafic and metamorphic rocks (Zhao and Cawood, 2012). The exposure of these deep crustal materials is ascribed to post-Mesozoic extrusion and associated east- and southeast-directed thrusting processes in the region, which are thought to result from the Mesozoic collision between the North China and South China blocks as well as Cenozoic India-Eurasia convergence (e.g., Wang and Meng, 2009). In addition, the Panxi-Hannan Belt sporadically hosts igneous rocks within the age range 970–900 Ma (Fig. 1A; Li et al., 2018; Wu et al., 2019). These rocks mostly display arc-like geochemistry and depleted mantle-like isotopic compositions and are thought to have formed within intra-oceanic arc settings (Li et al., 2018; Wu et al., 2019). Several intermediate-high grade metamorphic records within the period of 880–760 Ma have also been reported in the belt (Fig. 1A), including ca. 800 Ma amphibolite to granulite facies metamorphism in the northern part of the belt (Wang et al., 2020) and 880–760 Ma epidote amphibolite to amphibolite facies metamorphism in the southern part of the belt (Li et al., 2022; Yang et al., 2024).

The Pengguan Complex is one of largest basement units within the Panxi-Hannan Belt, comprising ca. 860–750 Ma plutonic rocks and metamorphic rocks of the Huangshuihe Group (Fig. 1B; Zhang et al., 2008; Yan et al., 2008). It is bounded by the Longmenshan Thrust faults and is tectonically overlain by deformed Sinian–Paleozoic sequences (Yan et al., 2008). Previous studies have shown that the Huangshuihe Group in this area experienced up to amphibolite facies metamorphism and that it consists of schist, plagioclase amphibolite, migmatite, and meta-volcanic rocks (BGMRSC, 1991). However, its geochronology and metamorphic histories have only been loosely constrained.

In this study, we investigated the Huangshuihe Group rocks occurring in the interior of the Pengguan Complex (Fig. 1B). The group is well-exposed in a section along a north–south river channel extending over 2 km in length (Fig. 1B). Massive high-angle, south-verging thrust faults have developed in the section, likely the result from post-Mesozoic tectonics (Fig. 1C; Wang and Meng, 2009). The section can be subdivided into northern and southern parts based on their different rock types, separated by a ~200 m-long diorite pluton (Fig. 1C). The north section is mainly characterized by stromatic migmatites (Fig. 1C), which develop foliation-parallel leucosome, melanosome, and mesosome and have sedimentary protoliths (Li et al., 2021a). The southern section comprises of layered and lens-shaped metasandstone and a series of granitic to gabbroic gneisses (Figs. 1C; S1). The gneisses generally enclose lenses of amphibolite, quartzite, and meta-tonalite. They are characterized by monomineralic banding and exhibit extensive deformation features, such as mylonite with S-C fabrics, cleavage, fault, and fold (Figs. 1C; S1). We collected two orthogneiss samples from the southern section (Fig. 1C–E).

3. Methods

The orthogneiss samples taken from the Huangshuihe Group were investigated using a combination of Tescan Integrated Mineral Analyzer (TIMA) mineral mapping, major element compositional analysis, zircon U–Pb–Hf–O isotopic analysis, zircon trace element analysis, and whole-rock Rb–Sr–Sm–Nd isotopic analysis. Extended methods are provided in Supplementary Text 1.

The TIMA analysis was conducted at Nanjing Hongchuang Geological Exploration Technology Service Co., Ltd. using a Mira-3 scanning electron microscope equipped with energy dispersive X-ray spectrometers (EDS, EDAX Element 30). The measurements were conducted in the dot mapping mode, which includes the collection of backscattered electron (BSE) and EDS data on a regular grid (9 μm dot spacing). The analyses were performed at 25 kV using a spot size of ~90 nm, and a working distance of 15 mm. Obtained whole TIMA maps are shown in Fig. S4. Based on the TIMA mineral mapping results, we calculated the mineral volume and mass proportion on the two samples (Table S1). Major element compositions and BSE images of plagioclase, amphibole, pyroxene, epidote, phengite, and chlorite grains were acquired using a JXA-8230 (JEOL) electron microprobe analyzer (EMPA) at the Testing Centre of the Shandong Bureau of China Metallurgy and Geology, Ji'nan, China. Operating conditions included a 15 kV accelerating voltage and a 2.0×10^{-8} A beam current. A beam size of 10 μm in spot mode was applied. The analytical precision (i.e., one standard deviation) for the major elements with mass proportions > 1 wt% was generally better than 2 % (Table S2). Representative BSE images are shown in Fig. S3 and the obtained EMPA data are shown in Table S2.

Zircon grains were separated using conventional density and magnetic techniques, mounted in epoxy resin disks, and polished to expose their grain surfaces. The internal structures of zircon were imaged using Cathodoluminescence (CL) techniques. The zircon U–Pb–O isotope analyses were acquired using a Cameca IMS-1280HR SIMS at the Guangzhou Institute of Geochemistry, Chinese Academy of Sciences, with detailed analytical procedures outlined in Supplementary Text 1. Zircon Lu–Hf isotopic analysis was conducted using a GeoLas 193 nm laser-ablation system attached to a Neptune (Plus) MC-ICP-MS at the State Key Laboratory for Mineral Deposits Research, Nanjing University (MiDeR-NJU), with detailed analytical procedures outlined in Supplementary Text 1.

Zircon core and rim trace element compositions were analyzed using the Cameca IMS-1300HR[3] SIMS also at MiDeR-NJU. A 5 nA primary O_2^- shaped beam was utilized to analyze the sample surface with 23 keV impact energy. The 20 μm raster was used to remove the gold coating, and the final work beam size was about 15 × 20 μm. Measurement was conducted in the mono-collector mode. The following masses sequences were measured: ^{48}Ti, ^{49}Ti, ^{89}Y, ^{139}La, ^{140}Ce, ^{141}Pr, ^{142}Nd, ^{147}Sm, ^{153}Eu, ^{158}Gd, ^{159}Tb, ^{163}Dy, ^{165}Ho, ^{167}Er, ^{169}Tm, ^{174}Yb, ^{175}Lu, ^{180}Hf, ^{238}U, and

^{232}Th. Each spot analysis includes 5 scan cycles. In order to separate the light-REE oxide interference, the > 15,000 mass resolving power was applied. The concentration data for zircons were standardized against the zircon standard 91,500 (Table 3 in Coble et al., 2018) which was analyzed repeatedly throughout the duration of the analytical session. Intensities were normalized to $^{90}Zr_2^{16}O$, stoichiometric compositions were assumed for zircon standards and unknowns. Measured 91,500 zircon had relative standard deviations of about ± 8–10 % for U and Th, ± 9 % for Ti, ± 3 % for Hf, ± 1–5 % for Y and HREEs (Table S3). Measured REE contents were normalized to the chondrite values of McDonough and Sun (1995).

4. Results

4.1. Petrography and mineral chemistry

Sample 15PG32–2 contains ~57 vol% amphibole (Amp), ~24 vol% albite (Ab), ~13 vol% phengite (Phe), ~5 vol% quartz (Q), and < 1 vol% of other phases in total [chlorite (Chl), epidote (Ep), garnet (Gt), orthoclase (Or), apatite, titanite, calcite, and zircon] (Table S1; Fig. 2;

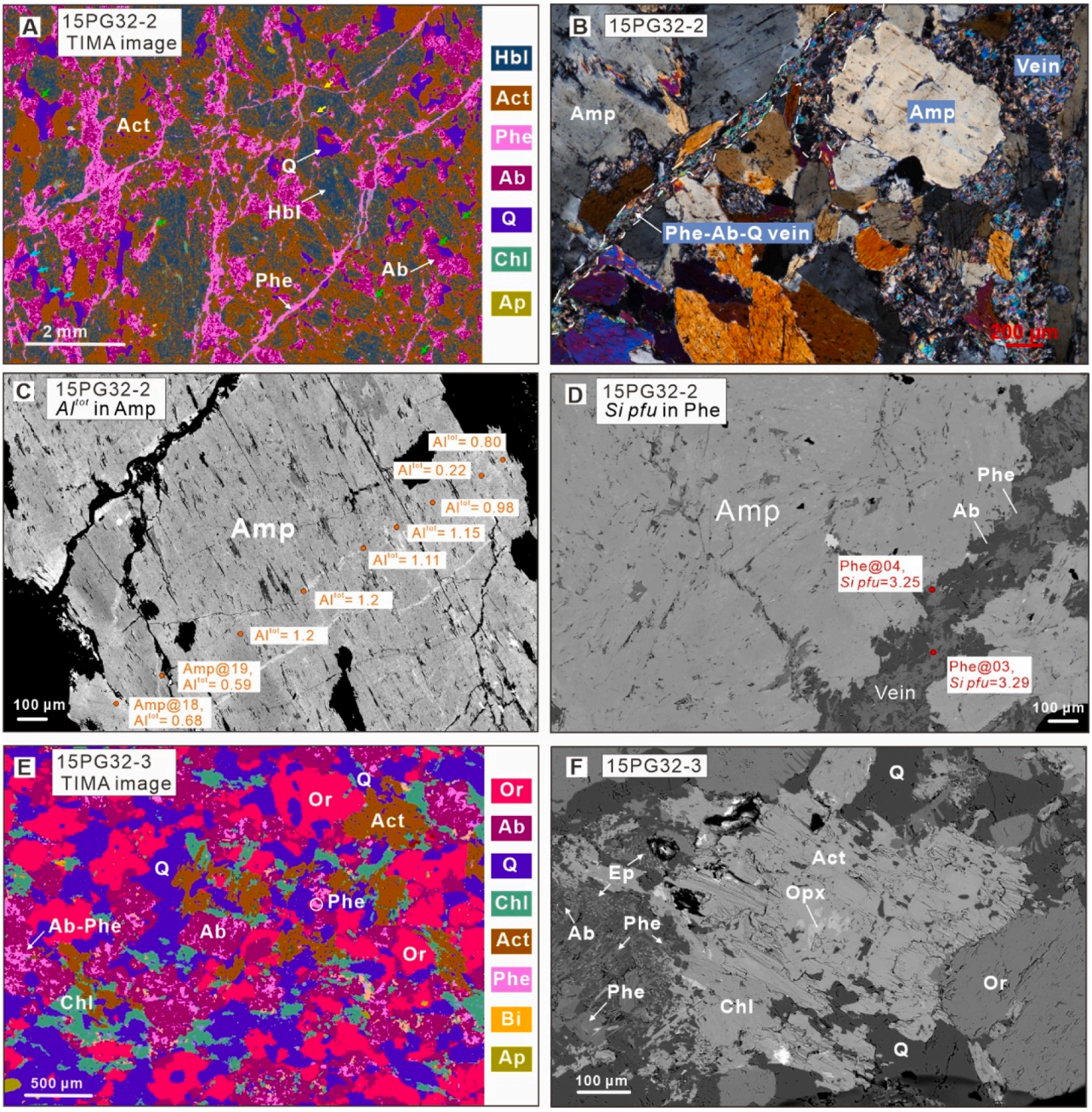

Fig. 2. Micrographic photographs showing the characteristics of samples. (A) TIMA mapping image of sample 15PG32–2. Green arrows denote the small dihedral angels of quartz and assemblage albite-phengite. Yellow arrows denote the pseudomorphs of melt film for assemblage albite-phengite. Cyan arrows denote the string-of-beads textures of quartz. (B) Photomicrograph of 15PG32–2 in cross-polarized light. (C) Typical amphibole (Amp) grain and its Al^{tot} *pfu* (marked in orange) variation under backscattered electron (BSE) imaging. "Amp@18″ and "Amp@19″ point to Data Numbers in Table S2. (D) BSE image showing veinlet mineral assemblage of phengite (Phe)-albite (Ab)-quartz (Q). Analyzed phengite domains and their *Si pfu* contents are labeled (red). "Phe@03″ and "Phe@04″ point to Data Numbers in Table S2. (E) TIMA mapping image for 15PG32–3. (F) BSE image of 15PG32–3 exhibiting the relict orthopyroxene (Opx) and coexistence of albite, epidote, and phengite.

Fig. S2–S4). The volume proportions of the minerals were determined by TIMA mineral mapping results (Table S1). The amphibole grains are subhedral to anhedral, partially corroded, and/or fragmented, and usually 1 to 3 mm in size (Fig. 2A–B). They exhibit variable compositions ranging from actinolite (Act) with Al^{tot} *pfu* (total aluminum content per formula unit calculated on the basis of 13 cations) of 0.05 to magnesio-hornblende (Hbl) with Al^{tot} *pfu* of 1.32 (Fig. 3A). The actinolite and hornblende generally intergrow with each other (Fig. 2A; Fig. S3G–H; Fig. S4A), and the amphibole exhibits a core-rim structure with hornblende-rich core and actinolite-rich rim (Fig. 2A&C; Fig. S2C; Fig. S3E–G). The actinolite thus potentially represents a partial overprint on the hornblende due to the metamorphic reaction (Grapes and Graham, 1978). The albite grains are anhedral except for a few lath-shaped grains, and they vary in size (0–5 mm) but have homogeneous compositions (An_{0-4}) (Table S2; Fig. 2A&D; Fig. S3K–L). Phengite is associated with albite, has a flaky morphology, tiny grain size (~50 μm in longest dimension), and a *Si pfu* ranging from 3.166 to 3.357 (atoms per formula unit; 3.287–3.357 *Si pfu* for 12 of 16 spots) (Fig. 2D, 3B; Fig. S3A–D). Two types of the albite-phengite assemblage occur in sample 15PG32–2. One exhibits melt-related microstructures (such as small dihedral angles and pseudomorphs of melt films) (Fig. 2A; Fig. S2A–B) and forms the semi- to inter-connected vein networks that cross-cut or surround amphibole grains (Fig. 2A–B). The other is large (~4 mm) and lath-shaped, possibly transformed from plagioclase (Pl) precursor (Fig. S2F, S3L). Epidote is tiny in size (< 50 μm in longest dimension) and occurs within albite (Fig. S3C). The quartz grains are anhedral, optically continuous, locally show melt-related microstructures (e.g., small dihedral angles and string of beads textures), and fill in grain boundaries or intra-grain fractures (Fig. 2A; Fig. S2A–B). The above features indicate that a large proportion of hornblende and some plagioclase likely served as precursor minerals, indicating a possible mafic protolith for the sample. Furthermore, the semi- to inter-connected vein structures and melt-related microstructures in the sample are interpreted as evidence of former presence of melt (see Sawyer, 1999; Holness and Sawyer, 2008; Vernon, 2011), now pseudomorphed by the albite-phengite-quartz association. The melt precursor accounts for ~45 vol% of the sample. We further interpret that the melt-mineral interaction led to the replacement of hornblende by actinolite and the plagioclase by albite-phengite-epidote association.

Sample 15PG32–3 contains ~30 vol% orthoclase (Or), ~29 vol% quartz, ~26 vol% albite, ~8 vol% chlorite, ~3 vol% phengite, ~1 vol% actinolite, and < 3 vol% of other phases in total [epidote, garnet, orthopyroxene (Opx), apatite, titanite, biotite, calcite, pyrite, allanite, zircon, and monazite] (Table S1; Fig. 2E–F; Fig. S2–S4). Albite grains vary in size (0–2 mm) but are homogeneous in composition (An_{1-7}; Table S2), and are partially corroded and/or fragmented (Fig. 2E; Fig. S4B). The larger grains (~1–2 mm) are generally subhedral to euhedral with a lath-shaped habit, in contrast to the smaller grains (< 1 mm) with anhedral morphologies (Fig. 2E; Fig. S4B). In particular, albite contains numerous inclusions of flaky and tiny phengite (50–100 μm in longest dimension; *Si pfu* of 3.121–3.367) and epidote (< 50 μm in longest dimension) (Fig. 2F; Fig. S2I; Fig. S3M–R). The albite-phengite-epidote assemblage in the sample is interpreted to be completely transformed from the plagioclase precursor (e.g., Oliot et al., 2010; Luisier et al., 2019; Schorn, 2022). Orthoclase and quartz grains either have embayed grain boundaries in contact with albite or enclose albite (Fig. 2E; Fig. S4B). Both are variable in size (0–3 mm) with anhedral morphologies and exhibit melt-related microstructures indicative of former melt, such as small dihedral angles and string-of-beads textures (Fig. S4B). Their assemblage forms an interconnected network within the sample (Fig. S4B). The actinolite and chlorite are closely associated with each other, and their assemblage expresses the foliation within the sample (Fig. S4B). The actinolite generally occurs as a prismatic aggregate and is partially rimmed by chlorite (Fig. 2F; Fig. S2G; Fig. S3S–X), potentially indicating that chlorite partially overprinted the actinolite. In addition, we found that minor fine-grained orthopyroxene relics with irregular grain shapes were enclosed by actinolite (Fig. 2F), indicating an overprinting of orthopyroxene by actinolite. According to the above features, we suggest that the plagioclase and orthopyroxene may serve as precursor mineral phases of the sample, hinting at a mafic protolith. An assemblage of orthoclase-quartz represents the pseudomorph of former melt and accounts for ~60 vol.% of the sample. This assemblage could be interpreted as a result of the penetration of felsic melt derived from an external source and treated as external leucosome. Furthermore, we interpret that the melt-mineral interaction led to the replacement of orthopyroxene by the actinolite-chlorite association and plagioclase by the albite-phengite-epidote association.

4.2. Zircon U–Pb–Hf–O isotopes and trace elements and whole-rock geochemistry

Zircon grains in the samples generally show core-rim (± mantle) structures under CL imaging (insets of Fig. 4A–B; Fig. S5). The zircon cores have irregular morphologies and Th/U ratios typically > 0.4 (Table S3), consistent with a magmatic origin. Their internal structures are quiet variable under CL imaging: those of 15PG32–2 display oscillatory zoning, broad zoning, sector zoning, or no zoning with varying levels of brightness; those of 15PG32–3 display broad zoning with dark CL intensity. The core domains may have been partially dissolved given their irregular morphologies and the occurrence of prominent bright-CL

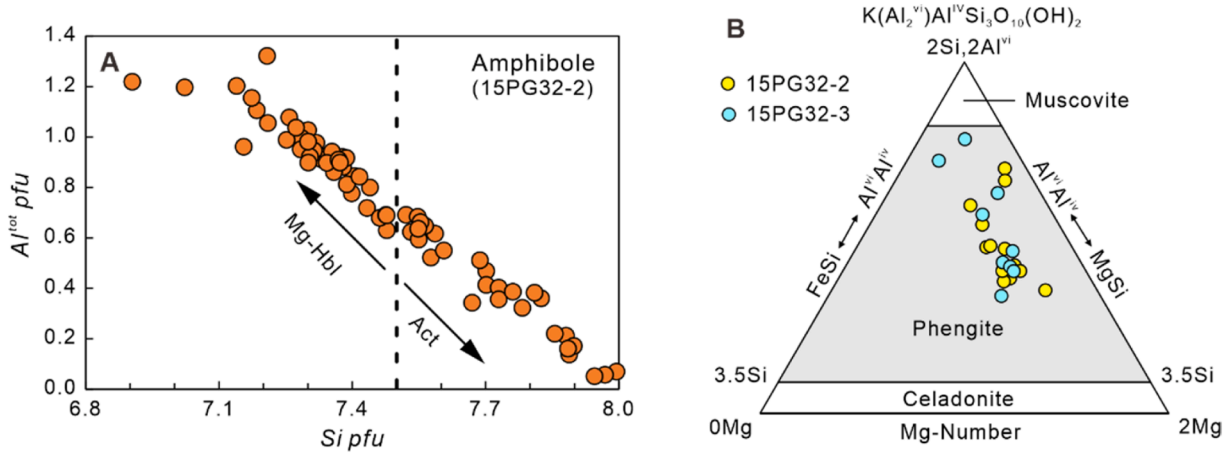

Fig. 3. Mineral compositions variations. (A) Al^{tot} *pfu* vs. *Si pfu* plot for all analyzed amphibole domains in 15PG32–2, indicating their variable compositions ranging from actinolite (Act) with Al^{tot} of 0.05 to magnesio-hornblende (Hbl) with Al^{tot} of 1.32. (B) Classification diagram (after Tappert et al., 2013) demonstrating that all analyzed mica domains in both samples belong to the phengite series.

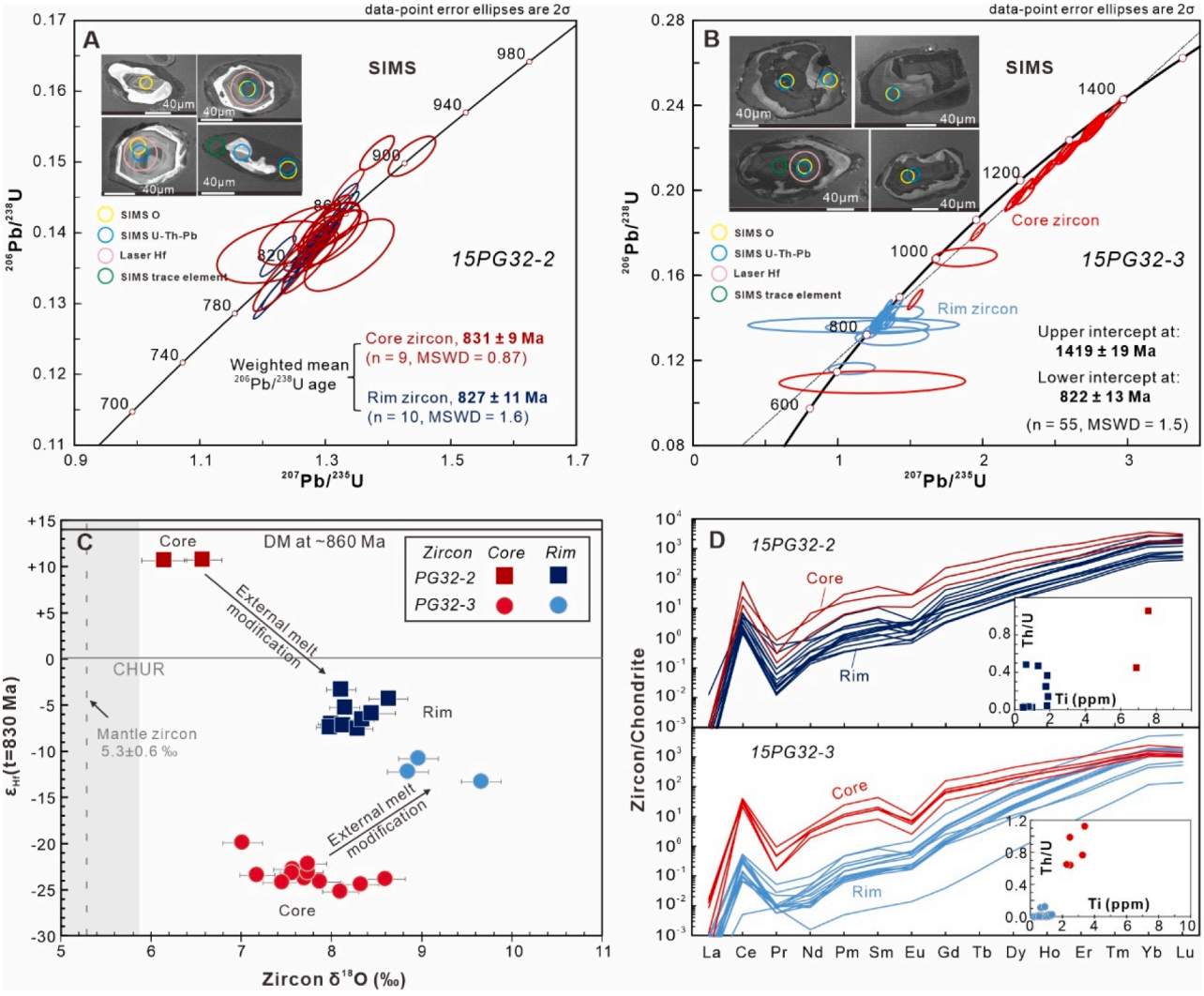

Fig. 4. Zircon U–Pb–Hf–O isotopes and trace elements for zircon core and rim domains of the two samples. (A–B) U–Pb concordia diagrams, with some representative zircon CL images inset. (C) zircon $\varepsilon_{Hf(t\ =\ 830\ Ma)}$ -$\delta^{18}O$ diagram showing the distinct isotopic compositions of core and rim domains. Error bars show two standard errors. The range of mantle zircon $\delta^{18}O$ of 5.3 ± 0.6 ‰ is from Valley et al. (2005). (D) Zircon chondrite-normalized REE distribution patterns with insets showing the plots of zircon Th/U ratios vs. Ti concentrations.

domains that separate cores and rims. The zircon rims generally exhibit no zoning with homogeneously dark CL intensity and Th/U ratios < 0.1 (Table S3) that are indicative of metamorphic origins.

We plotted the zircon dating results on U–Pb concordia diagrams (Fig. 4A, B). For sample 15PG32–2, ages of the zircon core and rim domains are generally indistinguishable and most fall within 860–820 Ma (Fig. 4A). We thus adopted weighted mean $^{206}Pb/^{238}U$ ages to represent their formation ages. We excluded the discordant ages and one abnormal age (ca. 905 Ma; 15PG32–2@35) (see Table S3 for criterion of age discordance), resulting in calculated weighted mean $^{206}Pb/^{238}U$ ages of 827 ± 11 Ma (n = 10, MSWD = 1.6) for zircon rim domains and 831 ± 9 Ma (n = 9, MSWD = 0.87) for zircon core domains (Fig. 4A). On the other hand, the analyzed zircon core domains have $\varepsilon_{Hf}(t)$ values of +10.1 and +10.4 (with two-stage Hf model ages of ca. 1.0 Ga; n = 2) and $\delta^{18}O$ values from 5.55 to 6.85 ‰ (n = 11), whereas the zircon rim domains have $\varepsilon_{Hf}(t)$ values of –7.6 to –3.4 (with two-stage Hf model ages ca. 1.9–2.2 Ga; n = 9) and $\delta^{18}O$ values from 7.99 to 9.04 ‰ (n = 19) (Fig. 4C; Table S3). For sample 15PG32–3, zircon core and rim dates fall into two distinct groups and yield a well-defined Discordia line (n = 55), with an upper intercept at 1419 ± 19 Ma and a lower intercept at 822 ± 13 Ma (MSWD = 1.5) (Fig. 4B). The upper and lower intercept ages may denote the timing of magma crystallization and metamorphism, respectively. Considering these intercept ages, the zircon core domains have $\varepsilon_{Hf}(t$ = 1419 Ma) values of –12.0 to –6.9 (with two-stage Hf model ages ca. 2.6–3.0 Ga; n = 13) and $\delta^{18}O$ values of 7.07 to 9.32 ‰ (n = 22), whereas the zircon rim domains have $\varepsilon_{Hf}(t$ = 822 Ma) values of –15.4 to –9.4 (with two-stage Hf model ages ca. 2.2–2.7 Ga; n = 9) and $\delta^{18}O$ values of 8.04 to 9.86 ‰ (n = 16) (Fig. 4C; Table S3).

For zircon trace elements of 15PG32–2, both core and rim domains show similar REE (rare earth element) patterns (i.e., depletions in light REE, enrichment in heavy REE, and negative Eu anomalies), while the core domains have higher Ti concentrations (6.88–12.8 ppm; n = 3) than rim domains (0.47–1.88 ppm for 14 analyses, 6.25 ppm and 15.8 ppm for 2 analyses) (Fig. 4D; Table S3). For zircon trace elements of 15PG32–3, rim domains exhibit lower concentrations of light REEs and Ti (0.22–1.31 ppm for 16 analyses, 2.53–8.11 ppm for 4 analyses) and less negative Eu anomalies (Eu/Eu* = 0.19–0.87, chondrite normalized $Eu/\sqrt{Sm * Gd}$) than the core domains (Ti = 2.29–3.38 ppm; Eu/Eu* = 0.15–0.29; n = 5) (Fig. 4D; Table S3).

As the Ti concentration of zircon is sensitive to temperature along with quadrivalent Ti substituting for Si (Ferry and Watson, 2007), we could apply the Ti-in-zircon thermometer from Ferry and Watson (2007) to the zircon rims to estimate metamorphic temperatures. The thermometer involves the activities of both TiO_2 and SiO_2 (α_{TiO2} and α_{SiO2})

in the rock systems, and the calculated Ti-in-zircon temperatures increase with α_{TiO2} and decrease with α_{SiO2}. The occurrence of abundant quartz in both samples enables us to assume $\alpha_{SiO2} = 1$ for the system. The minor Ti-bearing phase of titanite present in both samples led us to apply $\alpha_{TiO2} = 0.5–0.8$ in accordance with the literature (e.g., Barnes et al., 2019, and references therein). We excluded zircon rim analyses with high-Ti (> 2 ppm) concentrations from the calculation since they were either compositionally inhomogeneous or influenced by intra-grain fracture under CL imaging (see Table S3 for data filtering criterion). If $\alpha_{TiO2} = 0.8$, the calculated crystallization *T* for zircon rims is 535 ± 30 °C ~ 626 ± 36 °C for 15PG32–2 and 492 ± 28 °C ~ 600 ± 40 °C for 15PG32–3, with average values of 574 ± 74 °C ($n = 14$, 2SD) and 563 ± 57 °C ($n = 16$, 2SD). If $\alpha_{TiO2} = 0.5$, the calculated crystallization *T* for zircon rims is 563 ± 32 °C ~ 661 ± 38 °C for 15PG32–2 and 518 ± 29 °C ~ 634 ± 42 °C for 15PG32–3, with average values of 606 ± 79 °C ($n = 14$, 2SD) and 594 ± 61 °C ($n = 16$, 2SD). Overall, the metamorphic temperatures determined by Ti-in-rim zircon thermometry fall within range of 500–700 °C for both samples.

The measured whole rock major and trace elements and Rb–Sr and Sm–Nd isotopes are illustrated in Table S4. Both samples have enriched Sr–Nd isotopes, with $\varepsilon_{Nd(t\ =\ 830\ Ma)} = -9.0$ and $(^{87}Sr/^{86}Sr)_i = 0.708978$ for 15PG32–2, and $\varepsilon_{Nd(t\ =\ 830\ Ma)} = -16.8$ and $(^{87}Sr/^{86}Sr)_i = 0.706211$ for 15PG32–3.

4.3. Phase equilibria modeling

To determine the metamorphic *P-T* conditions, we utilized the Gibbs free energy minimization software *Perple_X 7.1.3* (Connolly, 2005) and the hp62ver.dat thermodynamic database (Green et al., 2016) to construct the equilibrium phase diagrams for both samples (Fig. 5). The calculations were carried out in the MnO—Na_2O—CaO-K_2O-FeO-MgO-Al_2O_3-SiO_2–H_2O—O_2 (MnNCKFMASHO) system. H_2O was treated as saturated, given the prevalence of hydrous phases in both samples. The O_2 contents represent the amount of Fe^{3+} and were calculated according to $2FeO + 0.5O_2 = Fe_2O_3$. Iron in both samples is predominantly found in amphibole, of which the Fe^{3+}/Fe^{2+} ratios (in mole) were determined through EMPA data (Table S2). In this regard, the O_2 values for modelling were calculated at 0.19 wt% for 15PG32–2 and 0.08 wt% for 15PG32–3. We selected solution models of cAmph(G), Pl(h), Pheng(HP), melt(HP), Gt(HP), Ep(HP), and Chl(HP) for 15PG32–2 and solution models of cAmph(G), Pl(h), Pheng(HP), melt(HP), Gt(HP), Ep(HP), Chl(HP), and Opx(HP) for 15PG32–3. The equilibrium mineral assemblage was inferred to be Hbl + Act + Phe + Ab + *Q* + Ep + Gt + Or + Chl in 15PG32–2 and Act + Phe + Ab + Or + Ep + *Q* + Gt + Chl in 15PG32–3. Chlorite was observed to occur locally along rim or cleavage planes of amphibole (Fig. 2A, F; Fig. S2G; Fig. S3S–X). As it may be a partial alteration product of amphibole during retrograde stage of metamorphism (i.e., greenschist facies overprinting), chlorite was not treated as a necessary equilibrium mineral phase of peak metamorphism. The orthopyroxene occurs as irregular core within actinolite and was regarded as the relict phase.

Next, since we suggested that this metamorphic system might have undergone infiltration of external melt and possible removal of melt (see discussion for details), we evaluated the influence of melt migration on the modelling results. We treated protolith rock plus external melt (i.e., of unknown composition) as an integrated unit. The composition of removed melt could roughly be compared to that of melt pseudomorph (e.g., 56 % albite + 32 % phengite + 12 % quartz in 15PG32–2). After

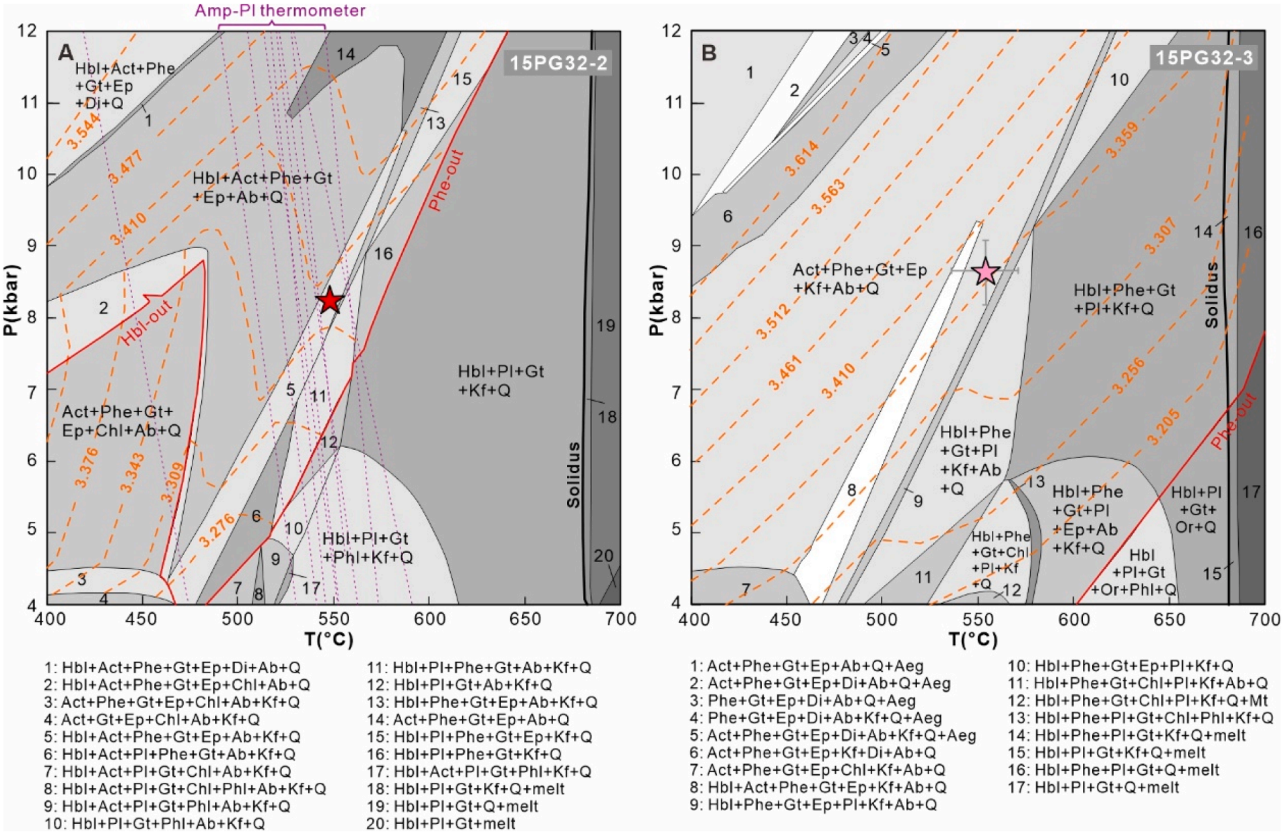

Fig. 5. Reconstructed peak *P-T* condition for the orthogneiss samples in the MnNCKFMASHO system (H_2O in excess). Predicted *Si*-in-phengite content isopleths are shown with orange dotted lines. (A) *P-T* pseudosection for sample 15PG32–2. Amphibole-plagioclase thermometer results (Holland and Blundy, 1994) are shown with purple dotted line. Red star represents peak metamorphism. (B) *P-T* pseudosection for sample 15PG32–3. Pink star represents peak metamorphism. Hbl – hornblende, Act – actinolite, Phe – Phengite, Gt – garnet, Ep – epidote, Ab – albite, Kf – K-feldspar, Q – quartz, Chl – chlorite, Pl – plagioclase, Mt – magnetite, Phl – phlogopite, Di – diopside, Aeg – aegirite.

several modelling tests (Supplementary Text 1), we found that the melt removed from the system had little influence on the modelled peak metamorphic *P-T* results. Therefore, we could adopt the measured bulk-rock composition as effective composition for modelling the metamorphic *P-T*. Modelling details are provided in the Supplementary Text 1.

After obtaining the *P-T* pseudosection, we combined equilibrium mineral assemblage, Ti-in-rim zircon temperatures (ca. 500–700 °C), amphibole-plagioclase thermometer (mostly 500–600 °C for 15PG32–2) (Fig. 5A; Holland and Blundy, 1994), Ti-in-amphibole thermometry (mostly 400–650 °C for 15PG32–2; Liao et al., 2021), and *Si*-in-phengite content isopleths (highest contents of 3.357 and 3.367 *pfu* for 15PG32–2 and 15PG32–3, respectively) to constrain peak metamorphic *P-T* conditions. This approach gave results of ~550 °C and ~8.2 kbar for 15PG32–2 and ~550 °C and ~8.6 kbar for 15PG32–3, which corresponds to a relatively cold (low *T/P* ratios) geothermal gradient of ca. 64–67 °C/kbar (or ca. 19.0–20.5 °C/km) (Fig. 5).

5. Discussion

5.1. Neoproterozoic low-T/P metamorphism accompanied by external melt infiltration

A combination of whole-rock, petrographic, and mineral geochemical analyses can provide insights on petrogenetic processes. We suggest that both samples from the western margin of Yangtze Block have mafic igneous protoliths since: (1) the zircon core domains of both samples exhibit consistent crystallization ages, Hf–O isotopes, and REE patterns (Fig. 4); and (2) their inferred precursor minerals are dominated by pyroxene/hornblende and plagioclase. Petrographically, the samples are characterized by corroded minerals (e.g., Amp in 15PG32–2; Ab in 15PG32–3) that indicate possible remelting, former presence of melt (pseudomorphed by Ab-Phe-Q veinlet in 15PG32–2 and Or-Q in 15PG32–3), abundant hydrous minerals (i.e., Amp, Phe, Chl, and Ep), and ubiquitous replacement microstructures (e.g., zircon core-rim structures, Hbl replacement by Act in 15PG32–3, and Pl replacement by Ab-Phe-Ep association). The zircon rims were crystallized at ca. 830–820 Ma and are systematically distinct from those of the core zircons with high-$\delta^{18}O$ (8.0–10‰) and low-$\varepsilon_{Hf}(t = 830\ Ma)$ (–3.4 to –15.3) (Fig. 4C). Thus, the protolith zircon has undergone a dissolution-recrystallization process with the presence of high-$\delta^{18}O$ and unradiogenic Hf isotopic melts at ca. 830–820 Ma. On the other hand, sample 15PG32–2 has a bulk-rock $\varepsilon_{Nd}(t = 830\ Ma)$ value of –9 (Table S4), which is considerably decoupled from Hf isotopes in zircon cores where $\varepsilon_{Hf}(t = 830Ma) = +10$. Since both samples that have igneous protoliths, in-situ melting and melt-mineral re-equilibration in closed systems was unlikely to have caused such large Hf–O isotopic variation from the zircon core to rim (Fig. 4C). Alternatively, the introduction of externally-derived melts that were potentially high-$\delta^{18}O$ and derived from ancient sources [as defined by the two-stage Hf model ages (ca. 1.9–2.7 Ga) of zircon rims] into the protolith rocks might be a more reasonable explanation.

On the other hand, a closed-system remelting might not be able to account for the presence of melt in both samples, since the temperatures of metamorphism and associated melt generation for the two samples were too low (500–600 °C based on mineral thermometers) to support a supra-solidus remelting in the closed systems (Fig. 5). The involvement of external melt is also supported by mineral chemistry and petrography. Both samples record the transformation of plagioclase to albite-phengite-epidote association following the reaction: plagioclase + melt (contains Mg, Fe, K) = albite + phengite + epidote. This reaction requires the introduction of magnesium, iron, and potassium to stabilize the epidote (measured FeO of 1.2–8.2 wt%) and phengite (measured FeO of 1.6–6.2 wt%, MgO of 0.8–5.7 wt%, K_2O of 8.4–11.7 wt%). For sample 15PG32–2, phengite has mass fraction of ~13 wt% and contributes in total ~1.5 wt% K_2O to the whole rock. In-situ melting of hornblende (K_2O generally < 0.5 wt%) and plagioclase precursors in a closed system could not supply such a large amount of K_2O from phengite. However, the introduction of K_2O from an external melt in an open system may be more plausible. In addition, the orthoclase-quartz association in 15PG32–3 was interpreted as a result of the penetration of felsic melt derived from an external source.

In summary, the protolith rocks have experienced the infiltration of external melts, remelting, former presence of melt, and pervasive mineral-melt interaction and re-equilibration at ca. 830–820 Ma. In general, the infiltration of melt and associated metasomatism are typically driven by tectonic events and are concomitant with changes in *P-T* conditions (i.e., metamorphism). Phengite (metamorphic white mica) occurs extensively in the two types of orthogneiss, either as a veinlet component or as metasomatic mineral, indicating that metamorphism most likely accompanied the melt infiltration. Therefore, the two orthogneiss samples, despite of their different protolith ages, underwent similar metamorphic histories.

5.2. Neoproterozoic accretionary orogenesis along WYB

Phengite, the principal mineral hosting H_2O, K_2O, and other mobile elements, is thought to be stable at low *T/P* conditions with pressure up to 10 GPa and temperature up to 1000 °C (Sorensen et al., 1997; Schmidt and Poli, 1998). It commonly forms in subducted oceanic crust (e.g., Schmidt and Poli, 2003; Hernández-Uribe and Palin, 2019), but can also be found within the accreted crust of convergent margins, such as the Mesozoic Franciscan accretionary complex along the western margin of the North American (Sorensen et al., 1997), and the ultrahigh-pressure metamorphic terrane within the Dabie-Sulu collisional orogen in central China (Zheng et al., 2003). In this study, the calculated metamorphic geothermal gradient (19.0–20.5 °C/km) is significantly lower than rift zones but is higher than the cold subducting slab top, consistent with either a warm subducting slab top or continental arc crust (Peacock, 1990; Rothstein and Manning, 2003; Hopkins et al., 2008) (Fig. 6A). The cold geotherm recorded by the Huangshuihe Group is incompatible with a mantle-plume regime, as plumes are expected to have temperatures of 100–300 °C above the ambient mantle, resulting in anomalously hotter geotherms than those in normal crust (Putirka, 2008; Koppers et al., 2021). We also rule out the possibility that the metamorphism occurred within subducting oceanic crust for the following reasons: (1) the igneous protolith of 15PG32–3 formed at ca. 1400 Ma with an Archean source precursor affinity (two-stage model Hf ages of 2.6–3.0 Ga for the zircon core domains; Table S3), indicating that it is most likely derived from continental crust material rather than oceanic crust material; (2) both samples have been hydrated through melt-rock interaction, as evidenced by the occurrence of abundant hydrous minerals (i.e., Amp, Phe, Chl, and Ep), which is not consistent with the dehydration process that usually occurs on the slab top.

The metamorphism more likely took place on the forearc side, since the protolith rock of 15PG32–3, with an age of ca. 1400 Ma, appears to originate from an outboard terrane that was accreted to the margin during convergent plate interaction (i.e., ongoing subduction; Yang et al., 2024). The rocks and detrital zircon of this age are largely lacking from the Yangtze Block. It was speculated that the outboard terrane sourced from central India or western Laurentia since such tectono-magmatic activity, although rare, was well developed in the ca. 1.4 Ga continental rifts of the two continents (Medig et al., 2014; Srivastava and Gautam, 2015). In addition, the migmatites (in the northern part of the studied section; Fig. 1C) near the sampled orthogneisses were interpreted to have the forearc sedimentary protoliths (Li et al., 2021a). Based on the above clues, we suggest that the metamorphism occurred either in the accretionary wedge of a warm subduction zone or in the overriding forearc continental crust (Fig. 6B). In either case, the metamorphism was facilitated by underthrusting processes along the subduction plane (the former case) or by intra-arc reverse faults (the latter case) (Ducea and Chapman, 2018). For the latter case, we further

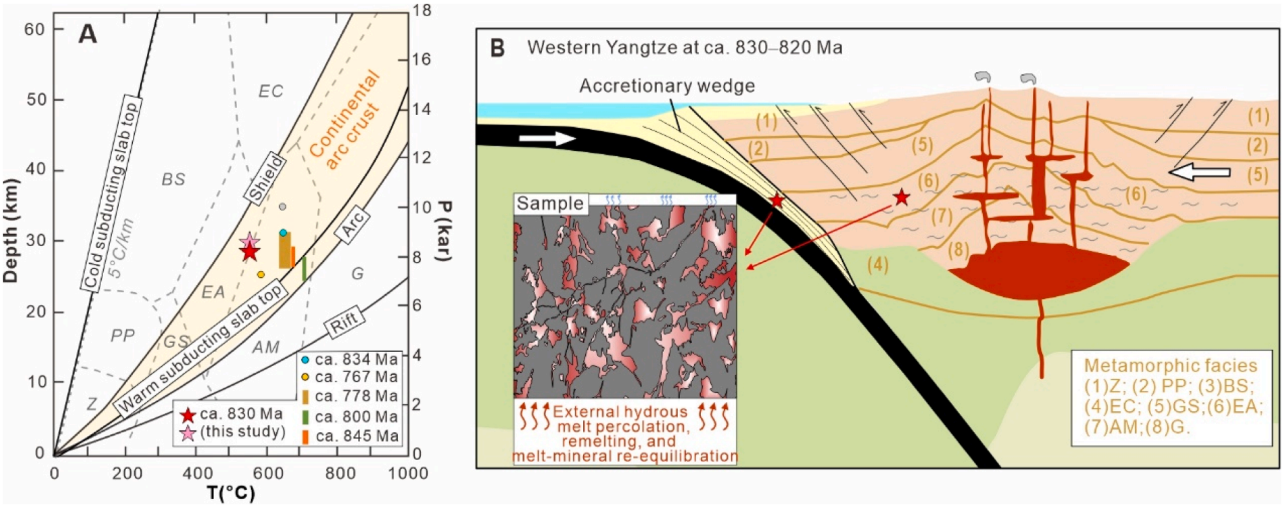

Fig. 6. Tectonic regime of the orthogneiss samples. (A) Peak metamorphic *P-T* condition of 15PG32–2 (red star) and 15PG32–3 (pink star) projected on geothermal gradients in various geologic settings and metamorphic facies (modified after Peacock,1990, Rothstein and Manning, 2003; Hopkins et al., 2008). Compiled Neoproterozoic peak metamorphic *P-T-t* records on the Panxi-Hannan Belt (Wang et al., 2020; Li et al., 2021b, 2022; Yang et al., 2024) are also plotted. Z – zeolite, PP – prehnite-pumpellyite, GS – greenschist, BS – blueschist, EA – epidote-amphibolite, AM – amphibolite, EC – eclogite, G – granulite. (B) Cartoon showing mid-Neoproterozoic ocean-continent subduction process along WYB (modified after Winter, 2014; Zhang et al., 2021). The samples (red stars) might have been located in the overriding forearc continental crust or an accretionary wedge of the subduction zone and suffered low-*T*/*P* metamorphism (EA facies) and the infiltration of external melt.

approximated the horizontal distance from the arc front to the metamorphic location using a one-dimensional heat conduction model in a semi-infinite body. The distance was calculated in range of ~30–60 km by assuming the arc magmas were not migrated and sustained 800 °C for ca. 10–30 m.y. (Fig. 7). In addition, an important question pertains to how the "low-*T*" orthogneisses were juxtaposed against the contemporaneous, "high-*T*", mafic–intermediate plutons (Fig. 1B). We suggest that the Neoproterozoic intra-arc (under)thrusting and exhumation processes may have facilitated the juxtaposition by inboard transportation of forearc materials. Alternatively, the post-Mesozoic thrusting process could also have played a role in this juxtaposition.

Overall, the low-*T*/*P* metamorphism at ca. 830–820 Ma on WYB

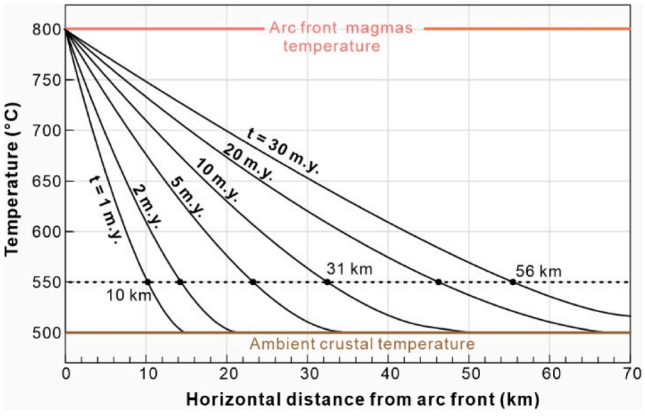

Fig. 7. Horizontal thermal conductivity simulation at ~30 km-deep continental magmatic arcs. The simulation was conducted in a semi-infinite body, assuming arc magmas were not migrated and had a constant temperature of ~800 °C while the ambient crust had an initial temperature of ~500 °C. *t* represents the duration time of the heating source. The duration time of arc magmas in this study was suggested to be ca. 10–30 m.y. since the continental arc magmatism in the studied area initiated at ca. 860–840 Ma and the metamorphism of this study was dated at ca. 830–820 Ma. To reach ~550 °C at ~30 km depth of the continental arc (the peak metamorphic condition of this study), the metamorphic location should be ~30–60 km far away from the arc front. More details for the simulation are provided in Supplementary Text 1.

likely occurred on the forearc side in the course of ocean-continent subduction (Fig. 6B). This subduction-orogeny model supports a hypothesis that the Yangtze Block was at the periphery of Rodinia (Cawood et al., 2018). However, this raises another important question why have subduction-diagnosed rocks of blueschists and "cold" eclogites not been found on WYB. On the one hand, this may result from poor preservation. The preservation of blueschist and cold eclogite requires the absence of retrograde fluids as well as a rapid exhumation (e.g., Matthews and Schliestedt, 1984; Avigad, 1993). However, the WYB might have experienced a tectonic transition from advancing to retreating orogenesis at ca. 800 Ma (see later discussion), resulting in a crustal geotherm change to higher *T*/*P*-ratio conditions that might facilitate metamorphic overprinting. On the other hand, the absence of blueschist may also be associated with the subduction geotherm-dependent dehydration of glaucophane (Bang et al., 2021). The glaucophane would persist to depths of ca. 240 km in cold subduction zones but would easily dehydrate and break down as shallow as ca. 40 km depths in warm subduction zones (Bang et al., 2021). If WYB underwent Neoproterozoic warm subduction, the blueschist would be hard to stabilize.

5.3. Implications for Rodinia's peripheral orogenesis during the Neoproterozoic

We combine zircon isotopic and the latest paleomagnetic data to evaluate the evolution of Neoproterozoic subduction zones of WYB (Fig. 8A, B) and explore the implications for Rodinia's peripheral orogenesis during the Neoproterozoic. The WYB was dominated by intra-oceanic subduction during the late-stage assembly of Rodinia (ca. 1000–900 Ma) (Fig. 8C; Li et al., 2018; Wu et al., 2019). Following its initial breakup at ca. 900 Ma, circum-Rodinia subduction systems started to expand (Cawood et al., 2021). Consequently, the Yangtze Block migrated away from a mantle upwelling and toward a mantle downwelling zone (Fig. 8C). This scenario might have been accompanied by a long-lived (at least ca. 900–750 Ma) continental arc system along WYB, given the following documented observations from the WYB and nearby regions: (1) both juvenile crustal addition and ancient crustal reworking at ca. 900–750 Ma in terms of zircon Hf isotopes (Fig. 8A); (2) a series of ca. 850–760 Ma intermediate-high grade metamorphic records (Fig. 6A); (3) rapid supracrustal recycling associated with intra-arc

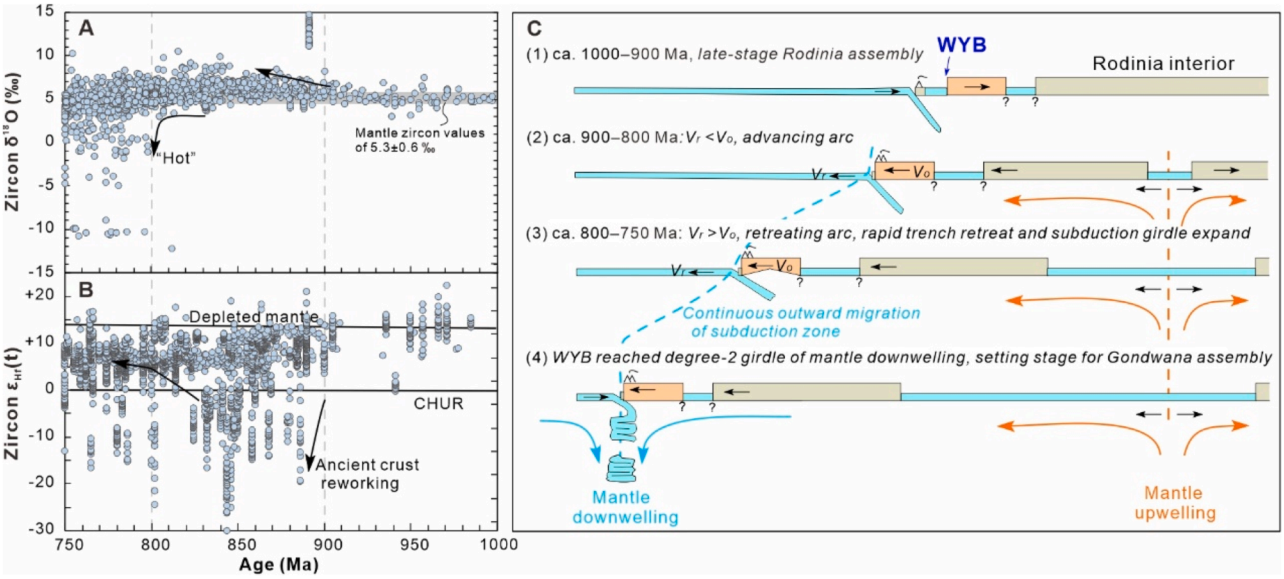

Fig. 8. Neoproterozoic orogenic evolution of WYB in context of Rodinia assembly and breakup. (A–B) Temporal variation of zircon Hf–O isotopes for the igneous rocks from WYB and its nearby region. Data are compiled from Wu et al. (2023) and Zhao et al. (2019, 2021). (C) Schematic cross section showing the continuous outward migration of the Yangtze Block from a mantle upwelling toward the degree-2 girdle of mantle downwelling (modified after Spencer et al., 2019), in response to Rodinia breakup. This scenario might have been accompanied by long-lived (at least ranging from ca. 900 Ma to ca. 750 Ma) convergent plate margin processes on WYB featuring alternating advance and retreate subduction orogeny.

underthrusting at ca. 820 Ma (Li et al., 2021); and (4) a range of igneous rocks with arc-like geochemistry (e.g., Zhao et al., 2021). Furthermore, we have revealed a transition of zircon isotopes at ca. 800 Ma (Fig. 8A, B) and suggest it is a response to the switch from advance to retreat of the arc system based on: (1) the arise of a large amount of ^{18}O- depleted zircon (with $\delta^{18}O$ lower than the mantle value) after ca. 800 Ma, possibly corresponding to a (locally) high-temperature, extensional environment (e.g., Zou et al., 2021); (2) zircon Hf isotopes showing a transition from being more continental-like to more mantle-like at ca. 800 Ma; and (3) paleomagnetic studies that demonstrate a fast movement of the Yangtze Block from ca. 800 Ma to ca. 760 Ma (Jing et al., 2021), which may reflect a rapid trench retreat and consequent outpacing of slab rollback from continental drift (i.e., retreating orogenesis) (Spencer et al., 2019). Therefore, we suggest the WYB displays a history of both advancing and retreating convergent plate margin processes during the early to middle Neoproterozoic (Fig. 8C). Upon the arrival of the Yangtze Block at the great cycle of mantle downwelling, it may have converged to form Gondwana over the locus of downwelling (Cawood et al., 2021; Wang et al., 2021; Martin et al., 2024).

Overall, the WYB may represent part of a long-lived subduction girdle (at least ca. 970–750 Ma) at the periphery of Rodinia, placing the supercontinent in an overall extensional regime resulting in its breakup and driving the transition to Gondwana assembly (Cawood et al., 2016, 2021). This peripheral orogen of Rodinia likely involved alternating advancing and retreating subduction orogeny during its ocean-ward migration, and it provides a snapshot of the evolution of a complete long-lived circum-Rodinian subduction girdle during the transition from Rodinia to Gondwana (Fig. 8C).

6. Conclusions

The phengite-bearing orthogneisses discovered on WYB document a low-*T*/*P* metamorphism with a cold geothermal gradient (19.0–20.5 °C/km) at ca. 830–820 Ma. The metamorphism took place in continental margin arc crust and was accompanied by external melt infiltration and associated remelting and melt-mineral re-equilibration. We found that the metamorphic sample with a ca. 1400 Ma protolith age is likely derived from an outboard terrane that was accreted to the margin during convergent plate interaction. This finding provides evidence for middle Neoproterozoic accretionary orogenesis. The WYB represents part of long-lived circum-Rodinia subduction systems that were necessary for Rodinia's ultimate breakup and transition to Gondwana assembly. It featured a long-timescale (at least ca. 900–750 Ma) outward migration of the subduction zone, accompanied by both advancing and retreating accretionary orogenesis.

CRediT authorship contribution statement

Jun-Yong Li: Investigation, Validation, Visualization, Funding acquisition, Writing – original draft. **Xiao-Lei Wang:** Conceptualization, Resources, Funding acquisition, Project administration, Supervision, Validation, Writing – review & editing. **Peter A. Cawood:** Conceptualization, Validation, Writing – review & editing. **Zhi-Dong Gu:** Investigation. **Yue Guan:** Methodology.

Declaration of competing interest

The authors declare that they have no known competing financial interests or personal relationships that could appear to influence the work reported in this paper.

Acknowledgments

This work was financially supported by the National Natural Science Foundation of China (Nos. 42025202 and 42202053), the China National Postdoctoral Program for Innovative Talents (BX20220148), the Australian Research Council (FL160100168), and the Fundamental Research Funds for the Central Universities (XJ2023003901). We thank Alex Webb for editorial handling and suggestions that improved the quality of this work. Dillon Brown and David Hernández-Uribe are thanked for detailed, enlightening, and critical reviews of the manuscript. We acknowledge useful discussion with Ming Tang and Yu Zhu that improved this manuscript. We thank Peng Wu for supplying compiled zircon U-Pb-Hf-O data, Ning Ding for phase equilibria modelling, and Di Wang, De-Hong Du, and Jia-Kai Zhang for their help with field works.

Supplementary materials

Supplementary material associated with this article can be found, in the online version, at doi:10.1016/j.epsl.2024.118678.

References

Ashwal, L., Demaiffe, D., Torsvik, T., 2002. Petrogenesis of Neoproterozoic granitoids and related rocks from the Seychelles: the case for an Andean-type arc origin. J. Petrol. 43, 45–83.

Avigad, D., 1993. Tectonic juxtaposition of blueschists and greenschists in Sifnos Island (Aegean Sea)—Implications for the structure of the Cycladic blueschist belt. J. Struct. Geol. 15, 1459–1469.

Bang, Y., Hwang, H., Kim, T., Cynn, H., Park, Y., Jung, H., Park, C., Popov, D., Prakapenka, V.B., Wang, L., Liermann, H.P., 2021. The stability of subducted glaucophane with the Earth's secular cooling. Nat. Commu. 12, 1496.

Barnes, C.G., Werts, K., Memeti, V., Ardill, K., 2019. Most granitoid rocks are cumulates: deductions from hornblende compositions and zircon saturation. J. Petrol. 60, 2227–2240.

BGMRSC (Bureau of Geology and Mineral Resources of Sichuan Province), 1991. Regional Geology of Sichuan Province. Geological Publishing House, Beijing.

Brown, M., Kirkland, C.L., Johnson, T.E., 2020. Evolution of geodynamics since the Archean: significant change at the dawn of the Phanerozoic. Geology 48, 488–492.

Cawood, P.A., Hawkesworth, C.J., 2014. Earth's middle age. Geology 42, 503–506.

Cawood, P.A., Strachan, R.A., Pisarevsky, S.A., Gladkochub, D.P., Murphy, J.B., 2016. Linking collisional and accretionary orogens during Rodinia assembly and breakup: implications for models of supercontinent cycles. Earth Planet. Sci. Lett. 449, 118–126.

Cawood, P.A., Pisarevsky, S.A., 2017. Laurentia-Baltica-Amazonia relations during Rodinia assembly. Precambrian Res. 292, 386–397.

Cawood, P.A., Zhao, G., Yao, J., Wang, W., Xu, Y., Wang, Y., 2018. Reconstructing South China in Phanerozoic and Precambrian supercontinents. Earth-Sci. Rev. 186, 173–194.

Cawood, P.A., Wang, W., Zhao, T., Xu, Y., Mulder, J.A., Pisarevsky, S.A., Zhang, L., Gan, C., He, H., Liu, H., Qi, L., Wang, Y., Yao, J., Zhao, G., Zhou, M.F., Zi, J.W., 2020. Deconstructing South China and consequences for reconstructing Nuna and Rodinia. Earth-Sci. Rev. 204, 103169.

Cawood, P.A., Martin, E.L., Murphy, J.B., Pisarevsky, S.A., 2021. Gondwana's interlinked peripheral orogens. Earth Planet. Sci. Lett. 568, 117057.

Cawood, P.A., Chowdhury, P., Mulder, J.A., Hawkesworth, C.J., Capitanio, F.A., Gunawardana, P.M., Nebel, O., 2022. Secular evolution of continents and the Earth system. Rev. Geophy. 60, e2022RG000789.

Coble, M.A., Vazquez, J.A., Barth, A.P., Wooden, J., Burns, D., Kylander-Clark, A., Jackson, S., Vennari, C.E., 2018. Trace element characterisation of MAD-559 zircon reference material for ion microprobe analysis. Geostand. Geoanal. Res. 42, 481–497.

Connolly, J.A., 2005. Computation of phase equilibria by linear programming: a tool for geodynamic modeling and its application to subduction zone decarbonation. Earth Planet. Sci. Lett. 236, 524–541.

Ducea, M.N., Chapman, A.D., 2018. Sub-magmatic arc underplating by trench and forearc materials in shallow subduction systems: a geologic perspective and implications. Earth Sci. Rev. 185, 763–779.

Ferry, J.M., Watson, E.B., 2007. New thermodynamic models and revised calibrations for the Ti-in-zircon and Zr-in-rutile thermometers. Contrib. Mineral. Petrol. 154, 429–437.

Ge, R.F., Zhu, W.B., Wilde, S.A., He, J.W., Cui, X., Wang, X., Zheng, B.H., 2014. Neoproterozoic to Paleozoic long-lived accretionary orogeny in the northern Tarim Craton. Tectonics 33, 302–329.

Grapes, R.H., Graham, C.M., 1978. The actinolite-hornblende series in metabasites and the so-called miscibility gap: a review. Lithos 11, 85–97.

Green, E.C.R., White, R.W., Diener, J.F.A., Powell, R., Holland, T.J.B., Palin, R.M., 2016. Activity–composition relations for the calculation of partial melting equilibria in metabasic rocks. J. Metamorp. Geol. 34, 845–869.

Gu, Z.D., Wei, Z., Yuan, M., 2014. Zircon SHRIMP U-Pb dating of basal granite and its geological significance in Weiyuan area of Sichuan Basin. Chin. J. Geol. 49, 202–213.

Hernández-Uribe, D., Palin, R.M., 2019. A revised petrological model for subducted oceanic crust: Insights from phase equilibrium modelling. J. Meta. Geol. 37, 745–768.

Holland, T., Blundy, J., 1994. Non-ideal interactions in calcic amphiboles and their bearing on amphibole-plagioclase thermometry. Contrib. Mineral. Petrol. 116, 433–447.

Holness, M.B., Sawyer, E.W., 2008. On the pseudomorphing of melt-filled pores during the crystallization of migmatites. J. Petrol. 49, 1343–1363.

Hopkins, M., Harrison, T.M., Manning, C.E., 2008. Low heat flow inferred from >4Gyr zircons suggests Hadean plate boundary interactions. Nature 456, 493–496.

Hynes, A., Rivers, T., 2010. Protracted continental collision—Evidence from the Grenville Orogen. Can. J. Earth Sci. 47, 591–620.

Jing, X., Evans, D.A., Yang, Z., Tong, Y., Xu, Y., Wang, H., 2021. Inverted South China: a novel configuration for Rodinia and its breakup. Geology 49, 463–467.

Johansson, Å., 2009. Baltica, Amazonia and the SAMBA connection—1000 million years of neighbourhood during the Proterozoic? Precambrian Res. 175, 221–234.

Koppers, A.A.P., Becker, T.W., Jackson, M.G., Konrad, K., Müller, R.D., Romanowicz, B., Steinberger, B., Whittaker, J.M., 2021. Mantle plumes and their role in Earth processes. Nat. Rev. Earth Environ. 2, 382–401.

Konopásek, J., Janoušek, V., Oyhantçabal, P.S.J., Ulrich, S., 2018. Did the circum-Rodinia subduction trigger the Neoproterozoic rifting along the Congo–Kalahari Craton margin? Int. J. Earth Sci. (Geol Rundsch) 107, 1859–1894.

Li, J.Y., Wang, X.L., Gu, Z.D., 2018. Early Neoproterozoic arc magmatism of the Tongmuliang Group on the northwestern margin of the Yangtze Block: implications for Rodinia assembly. Precambrian Res. 309, 181–197.

Li, J.Y., Tang, M., Lee, C.T.A., Wang, X.L., Gu, Z.D., Xia, X.P., Wang, D., Du, D.H., Li, L.S., 2021a. Rapid endogenic rock recycling in magmatic arcs. Nat. Commun. 12, 3533.

Li, X.H., Li, Z.X., Ge, W.C., Zhou, H.W., Li, W.X., Liu, Y., Wingate, M.T.D., 2003. Neoproterozoic granitoids in South China: crustal melting above a mantle plume at ca 825 Ma? Precambrian Res. 122, 45–83.

Li, Z.M., Chen, Y.C., Zhang, Q.W., Liu, J.H., Wu, C.M., 2021b. U-Pb dating of metamorphic monazite of the Neoproterozoic Kang-Dian Orogenic Belt, southwestern China. Precambrian Res. 361, 106262.

Li, Z.M., Chen, Y.C., Zhang, Q.W., Liu, J.H., Wu, C.M., 2022. P-T conditions and timing of metamorphism of the Yuanmou area, southern Neoproterozoic Kang-Dian Orogenic Belt, southwest China. Precambrian Res. 374, 106642.

Li, Z.X., Zhang, L.H., Powell, C.M., 1995. South China in Rodinia: part of the missing link between Australia–East Antarctica and Laurentia? Geology 23, 407–410.

Li, Z.X., Li, X.H., Kinny, P., Wang, J., 1999. The breakup of Rodinia: did it start with a mantle plume beneath South China. Earth Planet. Sci. Lett. 173, 171–181.

Li, Z.X., Bogdanova, S.V., Collins, A.S., Davidson, A., De Waele, B., Ernst, R.E., Fitzsimons, I.C.W., Fuck, R.A., Gladkochub, D.P., Jacobs, J., Karlstrom, K.E., Lu, S., Natapov, L.M., Pease, V., Pisarevsky, S.A., Thrane, K., Vernikovsky, V., 2008. Assembly, configuration, and break-up history of Rodinia: a synthesis. Precambrian Res. 160, 179–210.

Liao, Y., Wei, C., Rehman, H.U., 2021. Titanium in calcium amphibole: behavior and thermometry. Am. Mineral. 106, 180–191.

Luisier, C., Baumgartner, L., Schmalholz, S.M., Siron, G., Vennemann, T., 2019. Metamorphic pressure variation in a coherent Alpine nappe challenges lithostatic pressure paradigm. Nat. Commun. 10, 4734.

Martin, E.L., Cawood, P.A., Murphy, J.B., Nance, R.D., Heron, P.J., 2024. The tectonics of introversion and extroversion: redefining interior and exterior oceans in the supercontinent cycle. Geol. Soc. Lond. Spec. Pub. 542 https://doi.org/10.1144/SP542-2023-54.

Matthews, A., Schliestedt, M., 1984. Evolution of the blueschist and greenschist facies rocks of Sifnos, Cyclades, Greece. A stable isotope study of subduction-related metamorphism. Contrib. Mineral. Petrol. 88, 150–163.

McDonough, W.F., Sun, S.S., 1995. The composition of the Earth. Chem. Geol. 120, 223–253.

Medig, K.P.R., Thorkelson, D.J., Davis, W.J., Rainbird, R.H., Gibson, H.D., Turner, E.C., Marshall, D.D., 2014. Pinning northeastern Australia to northwestern Laurentia in the Mesoproterozoic. Precambrian Res. 249, 88–99.

Merdith, A.S., Collins, A.S., Williams, S.E., Pisarevsky, S., Foden, J.D., Archibald, D.B., Blades, M.L., Alessio, B.L., Armistead, S., Plavsa, D., Clark, C., Müller, R.D., 2017. A full-plate global reconstruction of the Neoproterozoic. Gondwana Res. 50, 84–134.

Murphy, J.B., Pisarevsky, S., Nance, R.D., 2013. Potential geodynamic relationships between the development of peripheral orogens along the northern margin of Gondwana and the amalgamation of West Gondwana. Mineral. Petrol. 107, 635–650.

Oliot, E., Goncalves, P., Marquer, D., 2010. Role of plagioclase and reaction softening in a metagranite shear zone at mid-crustal conditions (Gotthard Massif, Swiss Central Alps). J. Metamorp. Geol. 28, 849–871.

Peacock, S.M., 1990. Numerical simulation of metamorphic pressure-temperature-time paths and fluid production in subducting slabs. Tectonics 9, 1197–1211.

Putirka, K., 2008. Excess temperatures at ocean islands: implications for mantle layering and convection. Geology 36, 283–286.

Rothstein, D.A., Manning, C.E., 2003. Geothermal gradients in continental magmatic arcs; constraints from the eastern Peninsular Ranges Batholith, Baja California, Mexico. Geol. Soc. Am. Spec. Paper 374, 337–354.

Sawyer, E.W., 1999. Criteria for the recognition of partial melting. Phys. Chem. Earth (A) 24, 269–279.

Schmidt, M.W., Poli, S., 1998. Experimentally based water budgets for dehydrating slabs and consequences for arc magma generation. Earth Planet. Sci. Lett. 163, 361–379.

Schmidt, M.W., Poli, S., 2003. Generation of mobile components during subduction of oceanic crust. Treat. Geochem. 3, 567–591.

Schorn, S., 2022. Self-induced incipient 'eclogitization' of metagranitoids at closed-system conditions. J. Metamorp. Geol. 40, 1271–1290.

Shu, L.S., Yao, J.L., Wang, B., Faure, M., Charvet, J., Chen, Y., 2021. Neoproterozoic plate tectonic process and Phanerozoic geodynamic evolution of the South China Block. Earth-Sci. Rev. 216, 103596.

Spencer, C.J., Murphy, J.B., Hoiland, C.W., Johnston, S.T., Mitchell, R.N., Collins, W.J., 2019. Evidence for whole mantle convection driving Cordilleran tectonics. Geophys. Res. Lett. 46, 4239–4248.

Spencer, C.J., Mitchell, R.N., Brown, M., 2021. Enigmatic mid-Proterozoic orogens: hot, thin, and low. Geophy. Res. Lett. 48, e2021GL093312.

Sobolev, S.V., Brown, M., 2019. Surface erosion events controlled the evolution of plate tectonics on Earth. Nature 570, 52–57.

Sorensen, S.S., Grossman, J.N., Perfit, M.R., 1997. Phengite-hosted LILE enrichment in eclogite and related rocks: implications for fluid-mediated mass transfer in subduction zones and arc magma genesis. J. Petrol. 38, 3–34.

Srivastava, R.K., Gautam, G.C., 2015. Geochemistry and petrogenesis of Paleo–Mesoproterozoic mafic dyke swarms from northern Bastar craton, central

India: geodynamic implications in reference to Columbia supercontinent. Gondwana Res. 28, 1061–1078.
Stern, R.J., 2018. The evolution of plate tectonics. Philos. Trans. R. Soc. A 376, 20170406.
Stern, R., 2020. The Mesoproterozoic single-lid tectonic episode: prelude to modern plate tectonics. GSA Today 30, 4–10.
Tang, M., Chu, X., Hao, J., Shen, B., 2021. Orogenic quiescence in Earth's middle age. Science 371, 728–731.
Tappert, M.C., Rivard, B., Giles, D., Tappert, R., Mauger, A., 2013. The mineral chemistry, near-infrared, and mid-infrared reflectance spectroscopy of phengite from the Olympic Dam IOCG deposit, South Australia. Ore Geol. Rev. 53, 26–38.
Valley, J.W., Lackey, J.S., Cavosie, A.J., Clechenko, C.C., Spicuzza, M.J., Basei, M.A.S., Bindeman, I.N., Ferreira, V.P., Sial, A.N., King, E.M., Peck, W.H., Sinha, A.K., Wei, C. S., 2005. 4.4 billion years of crustal maturation: oxygen isotope ratios of magmatic zircon. Contrib. Mineral. Petrol. 150, 561–580.
Vernon, R.H., 2011. Microstructures of melt-bearing regional metamorphic rocks. Geol. Soc. Am. Mem. 207, 1–11.
Wang, C., Mitchell, R.N., Murphy, J.B., Peng, P., Spencer, C.J., 2021. The role of mega-continents in the supercontinent cycle. Geology 49, 402–406.
Wang, E.C., Meng, Q.R., 2009. Mesozoic and Cenozoic tectonic evolution of the Longmenshan fault belt. Sci China Ser. D 52, 579–592.
Wang, H.Z., Oscar, L., Zhang, H.F., Zhang, H., Chen, X., Zhai, M.G., 2020. Recognition and significance of c. 800 Ma upper amphibolite to granulite facies metamorphism in metasedimentary rocks from the NW margin of the Yangtze Block. J. Geol. Soc. 177, 424–441.
Wang, X.L., Zhou, J.C., Griffin, W.L., Wang, R.C., Qiu, J.S., O'Reilly, S.Y., Xu, X.S., Liu, X. M., Zhang, G.L., 2007. Detrital zircon geochronology of Precambrian basement sequences in the Jiangnan orogen: dating the assembly of the Yangtze Cathaysia blocks. Precambrian Res. 159, 117–131.
Winter, J.D., 2014. Principles of Igneous and Metamorphic Petrology, 2nd Ed. Pearson Education Limited, England.
Wu, P., Zhang, S.B., Zheng, Y.F., Fu, B., Liang, T., 2019. Amalgamation of South China into Rodinia during the Grenvillian accretionary orogeny: geochemical evidence from Early Neoproterozoic igneous in the northern margin of the South China Block. Precambrian Res. 321, 221–243.
Wu, P., Zhang, S.B., Li, Z.X., Wu, Y.B., Zheng, Y.F., 2023. Secular change in the nature of mantle and tectonic evolution of northwestern margin of the Yangtze Block during Neoproterozoic: constraints from the mafic intrusions and associated granitoids of the Hannan and Xiaomoling complexes. Precambrian Res. 393, 107094.
Yan, D.P., Zhou, M.F., Wei, G.Q., Gao, J.F., Liu, S.F., Xu, P., Shi, X.Y., 2008. The Pengguan tectonic dome of Longmenshan Mountains, Sichuan Province: mesozoic denudation of a Neoproterozoic magmatic arc-basin system. Sci. China, Ser. D 51, 1545–1559.
Yang, Z., Cawood, P.A., Zi, J.W., Gou, L.L., Liu, G.C., Liu, R., Xu, X.F., 2024. Mid-Neoproterozoic (ca. 845 Ma) metamorphism of the southwestern Yangtze Block and its tectonic implications. Precambrian Res. 400, 107267.
Zhang, P., Zhou, Z.Y., Xu, C.H., Zhang, Q., 2008. Geochemistry of Pengguan complex in the Longmenshan region, western Sichuan province, SW China: petrogenesis and tectonic implications. Geotect. Metall. 32, 105–116.
Zhang, Z.M., Ding, H.X., Dong, X., Tian, Z.L., Du, J.X., 2021. Metamorphism and tectonic mechanisms of subduction zones. Acta Petrol. Sin. 31, 3377–3398.
Zhao, G.C., Cawood, P.A., 2012. Precambrian geology of China. Precambrian Res. 222–223, 13–54.
Zhao, J.H., Pandit, M.K., Wang, W., Xia, X.P., 2018. Neoproterozoic tectonothermal evolution of NW India: evidence from geochemistry and geochronology of granitoids. Lithos 316–317, 330–346.
Zhao, J.H., Zhou, M.F., Wu, Y.B., Zheng, J.P., Wang, W., 2019. Coupled evolution of Neoproterozoic arc magmatism and mantle wedge in the western margin of the South China Craton. Contrib. Mineral. Petrol. 174, 1–16.
Zhao, J.H., Nebel, O., Johnson, T.E., 2021. Formation and evolution of a Neoproterozoic continental magmatic arc. J. Petrol. 62 egab029.
Zheng, Y.F., Zhang, S.B., 2007. Formation and evolution of Precambrian continental crust in South China. Chin. Sci. Bull. 52, 1–12.
Zheng, Y.F., Fu, B., Gong, B., Li, L., 2003. Stable isotope geochemistry of ultrahigh pressure metamorphic rocks from the Dabie-Sulu orogen in China: implications for geodynamics and fluid regime. Earth-Sci. Rev. 62, 105–161.
Zhong, S.J., Zhang, N., Li, Z.X., Roberts, J.H., 2007. Supercontinent cycles, true polar wander, and very long-wavelength mantle convection. Earth Planet. Sci. Lett. 261, 551–564.
Zhou, M.F., Yan, D.P., Kennedy, A.K., Li, Y., Ding, J., 2002. SHRIMP U–Pb zircon geochronological and geochemical evidence for Neoproterozoic arc-magmatism along the western margin of the Yangtze Block, South China. Earth Planet. Sci. Lett. 196, 51–67.
Zhu, Y., Lai, S.C., Xie, W.L., Qin, J.F., Zhu, R.Z., Zhao, S.W., Liu, M., Zhang, F.Y., Zhang, Z.Z., Yang, H., 2023. Wet calc-alkaline magmatic fractionation in the middle−upper crustal sections of the continental arc: insights from the Neoproterozoic Nanba intrusive complex, western Yangtze Block, South China. 10.1130/B36786.1.
Zou, H., Li, Q.L., Bagas, L., Wang, X.C., Chen, A.Q., Li, X.H., 2021. A Neoproterozoic low-$\delta^{18}O$ magmatic ring around South China: implications for configuration and breakup of Rodinia supercontinent. Earth Planet. Sci. Lett 575, 117196.